Geophys. J. Int. (2007) **171,** 71–86 doi: 10.1111/j.1365-246x.2007.03481.x

Adaptive unstructured grid finite element simulation of two-dimensional magnetotelluric fields for arbitrary surface and seafloor topography

Antje Franke, Ralph-Uwe Börner and Klaus Spitzer

Institute of Geophysics, Technische Universität Bergakademie Freiberg Gustav-Zeuner-Stra βe 12, D-09596 *Freiberg, Germany.*
E-mail: franke@geophysik.tu-freiberg.de

Accepted 2007 April 29. Received 2007 April 23; in original form 2006 June 19

SUMMARY

We present an adaptive unstructured triangular grid finite element approach for effectively simulating plane-wave diffusive electromagnetic fields in 2-D conductivity structures.

The most striking advantage of irregular grids is their potential to incorporate arbitrary geometries including surface and seafloor topography. Adaptive mesh refinement strategies using an *a posteriori* error estimator yield most efficient numerical solutions since meshes are only refined where required.

We demonstrate the robustness of this approach by comparison with analytical solutions and previously published numerical simulations. Maximum errors may systematically be reduced to, for example, 0.8 per cent for the apparent resistivity and 0.2° in the phase.

An additional accuracy study of the thickness of the air layer in E-polarization suggests to keep a minimum thickness depending on lateral conductivity contrasts within the earth.

Furthermore, we point out the new quality and flexibility of our simulation technique by addressing two marine magnetotelluric applications. In the first case, we discuss topographic effects associated with a synthetic sinusoidal sea bottom model and in the second case, we show a close-to-reality scenario using real bathymetry data from the East Pacific Rise at 17°S.

Key words: adaptive unstructured grids, electromagnetics, electromagnetic modelling, finite element methods, marine topography.

1 INTRODUCTION

While the finite element method incorporating adaptive unstructured grids has been applied to engineering electromagnetics for years (e.g. Webb 1995; McFee & Giannacopoulos 2001), the numerical simulation of geo-electromagnetic applications has generally been carried out using straightforward discretizations of the fundamental partial differential equations. Most of the classical approaches such as the finite difference (FD), integral equation (IE) or finite element (FE) method, have largely applied rectangular grids to numerically compute the desired solutions. Especially, FD techniques approximate the electromagnetic fields in rectangular cells to which piecewise constant parameters, namely the electric conductivity σ, the magnetic permeability μ and the dielectric permittivity ε, are assigned. Jones & Price (1970) described an FD algorithm for 2-D modelling of electromagnetic fields including its application to a vertical discontinuity in electrical conductivity. Jones & Pascoe (1971) presented a more general computer program to calculate electromagnetic fields in an arbitrary 2-D environment. Brewitt-Taylor & Weaver (1976) provided a revision of the theory for 2-D FD approximations with respect to an extension towards 3-D modelling which was later introduced by Mackie *et al.* (1993). Aprea *et al.* (1997) published an improvement to FD approaches regarding arbitrary model geometries. They presented a formulation that provides more flexibility in the parametrization of the discretized region by dividing rectangular cells into two triangles of possibly different electrical conductivities. However, FD techniques are severely limited when curved boundaries are to be discretized (Holland 1993).

The IE method was rapidly developed from 2-D applications (Hohmann 1971) to the 3-D formulation (Raiche 1974; Hohmann 1975; Weidelt 1975; Wannamaker *et al.* 1984). However, the IE method requires the expensive computation of Green's functions and is limited to rather simple model classes. Hence nowadays, IE approaches are mainly applied to verify the results of other numerical modelling techniques.

The application of the FE technique to geo-electromagnetic modelling was first established by Coggon (1971). Using triangular elements in conjunction with non-uniform grids, a much more flexible mapping of structural boundaries including surface topography may be achieved. However, for the sake of simplicity, Fox *et al.* (1980) as well as Wannamaker *et al.* (1987) implemented 2-D FE formulations on regularly structured grids by decomposing rectangles into triangles. To a certain degree, they are applicable for the treatment of topography Wannamaker *et al.* (1987) and useful for

systematic studies of its effects on data (Fox *et al.* 1980). Reddy & Rankin (1975) developed a 2-D algorithm using quadrilateral elements. Orthogonal hexahedral meshes were applied by Li (2000) and Mitsuhata & Uchida (2004). Thus, the full power of such discretization techniques has not unfolded so far in the field of geoelectromagnetic modelling. There is, however, a wide range of engineering applications demonstrating the potential of the FE method.

We present a 2-D FE algorithm for modelling electromagnetic fields using adaptive unstructured grids. This discretization technique allows for arbitrary model geometries including surface topography (Franke *et al.* 2004). Our approach benefits from many advantages the FE method offers. Adaptive mesh refinement generally provides an optimization of both run time and accuracy. Based on an *a posteriori* error estimator grid cells are adjusted only where required.

Our algorithm has proved to yield satisfying results in comparison to analytical solutions and numerical computations for the 2-D comparison of modelling methods for electromagnetic induction (COMMEMI) models (Weaver & Zhdanov 1997). In this paper, the results computed by our code are compared with those calculated by an FE approach by Li (2000) and an FD algorithm by Weaver (1994) for the 2D-4 COMMEMI model.

We intend to show the advantages of our approach by studying models with surface and seafloor topography. Initially, several terrain correction methods were proposed to reduce the influence of surface undulations on data, for example, by Chouteau & Bouchard (1988) and Jiracek *et al.* (1989). These methods operate rather approximative. Their accuracy is hard to assess and they may fail for complicated terrain. Our approach strictly obeys the physics and thus gives reliable results for any terrain. In recent publications, topographic effects were reported to be of special interest in the emerging field of marine electromagnetic applications. Baba & Seama (2002) transformed the undulation of the seafloor into an appropriate change of electrical conductivity and magnetic permeability of a corresponding flat seabottom. The applicability of our approach to seafloor magnetotellurics will be demonstrated using a model that was recently described by Schwalenberg & Edwards (2004) who introduced an analytical formulation to calculate electromagnetic fields and impedances at sinusoidal interfaces. Finally, we show the capability of unstructured triangular grids to precisely parametrize a mid-oceanic ridge model from the Mantle Electromagnetic and Tomography (MELT) experiment (Evans *et al.* 1999) including real bathymetry data. Our numerical studies demonstrate severe effects on the data associated with the seafloor topography.

2 ELECTROMAGNETIC INDUCTION IN 2-D MEDIA

The behaviour of plane-wave time-harmonic diffusive electromagnetic fields is governed by Maxwell's equations. Neglecting displacement currents and assuming an $e^{i\omega t}$ time dependency with angular frequency ω, time t and the imaginary unit $i^2 = -1$ for the electric and the magnetic field vectors $\mathbf{E}$ and $\mathbf{H}$, respectively, they are given by:

$$\nabla \times \mathbf{H} = \sigma \mathbf{E}, \tag{1}$$

$$\nabla \times \mathbf{E} = -i\omega\mu \mathbf{H}, \tag{2}$$

where $\sigma = \sigma(x, z)$ denotes the electric conductivity. The magnetic permeability μ is understood as the free space permeability $\mu = \mu_0 = 4\pi \times 10^{-7} \frac{Vs}{Am}$.

Let y be the strike direction of a 2-D conductivity structure. We consider a right-handed coordinate system with the z-axis pointing positive upwards. In the 2-D case, eqs (1) and (2) reduce to

$$\frac{\partial H_x}{\partial z} - \frac{\partial H_z}{\partial x} = \sigma E_y, \tag{3}$$

$$-\frac{\partial E_y}{\partial z} = -i\omega\mu H_x, \tag{4}$$

$$\frac{\partial E_y}{\partial x} = -i\omega\mu H_z, \tag{5}$$

$$-\frac{\partial H_y}{\partial z} = \sigma E_x \tag{6}$$

$$\frac{\partial H_y}{\partial x} = \sigma E_z, \tag{7}$$

$$\frac{\partial E_x}{\partial z} - \frac{\partial E_z}{\partial x} = -i\omega\mu H_y \tag{8}$$

for a homogeneous region of conductivity σ. The occurrence of the field components E_y, H_x and H_z in eqs (3)–(5) is referred to as E-polarization, whereas eqs (6)–(8) hold for the case of H-polarization.

Once the strike-parallel components E_y and H_y have been computed, the remaining components H_x, H_z, E_x and E_z can be derived from eqs (4) to (7) by numerical differentiation in a subsequent procedure which is generally referred to as post-processing. From the horizontal electric and magnetic fields, the magnetotelluric impedances

$$Z_{xy} = \frac{E_x}{H_y} \quad \text{and} \quad Z_{yx} = \frac{E_y}{H_x} \tag{9}$$

yield the apparent resistivities

$$\rho_{xy} = \frac{1}{\omega\mu}|Z_{xy}|^2 \quad \text{and} \quad \rho_{yx} = \frac{1}{\omega\mu}|Z_{yx}|^2 \tag{10}$$

as well as the phases

$$\phi_{xy} = \arg(Z_{xy}) \quad \text{and} \quad \phi_{yx} = \arg(Z_{yx}). \tag{11}$$

Furthermore, the ratio of vertical to horizontal magnetic field components provides the magnetic transfer functions.

3 BOUNDARY VALUE PROBLEM

The combination of eqs (3)–(8) yields two decoupled second-order partial differential equations for the bounded region $\Omega \subset \mathbb{R}^2$ which have the general form

$$-\nabla \cdot (c\nabla u) + au = 0 \quad \text{in} \quad \Omega \tag{12}$$

for the strike-parallel components E_y and H_y. The parameters c, a and u have different representations depending on the polarization of the induced fields:

E-polarization:

$$u := E_y, \quad c := 1, \quad a := i\omega\mu\sigma, \tag{13}$$

H-polarization:

$$u := H_y, \quad c := 1/\sigma, \quad a := i\omega\mu, \tag{14}$$

To solve for the desired unknowns, appropriate boundary conditions need to be introduced. At internal boundaries Γ_{int} representing jumps between regions of the piecewise constant model

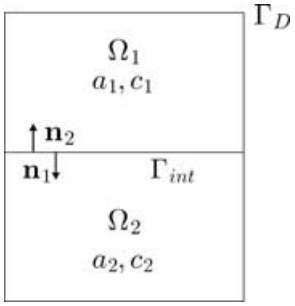

Figure 1. Domain $\Omega = \Omega_1 \cup \Omega_2$ with the outer Dirichlet boundary Γ_D, the inner boundary Γ_{int}, the pde coefficients a_i, $c_i (i=1, 2)$ and the outward unit normal vectors $\mathbf{n}_i (i=1, 2)$ on Γ_{int}.

parameter σ the tangential field components $\mathbf{n} \times (H_x, 0, H_z)^T$ and $\mathbf{n} \times (E_x, 0, E_z)^T$ are required to be continuous

$$\mathbf{n_1} \cdot c_1 \nabla u_1 + \mathbf{n_2} \cdot c_2 \nabla u_2 = 0 \quad \text{on} \quad \Gamma_{\text{int}}, \tag{15}$$

where $\mathbf{n}_i$ are the outward unit normal vectors and u_i is $E_{y,i}$ and $H_{y,i}$, respectively. To the outer boundaries Γ_D inhomogeneous Dirichlet boundary conditions of the form

$$u = r(x, z) \quad \text{on} \quad \Gamma_D \tag{16}$$

are assigned as a function r of the coordinates x and z. Exact analytical solutions are available for the horizontally layered half-space (Wait 1953). Taking into account that the stratification may be different at the left- and the right-hand side model margins, the electromagnetic field values at the horizontal upper and lower boundaries are obtained by a cubic spline interpolation.

Considering the simple model in Fig. 1, the boundary value problem is

$$-\nabla \cdot (c \nabla u) + au = 0 \quad \text{in} \quad \Omega_1, \Omega_2, \tag{17}$$

$$u = r(x, z) \quad \text{on} \quad \Gamma_D, \tag{18}$$

$$\mathbf{n}_1 \cdot c_1 \nabla u_1 + \mathbf{n}_2 \cdot c_2 \nabla u_2 = 0 \quad \text{on} \quad \Gamma_{\text{int}} \tag{19}$$

with u_1 and u_2 being the limits of u approaching the boundary Γ_{int} from Ω_1 and Ω_2, respectively.

4 FINITE ELEMENT METHOD

We seek for a solution u of the boundary value problem described by eqs (17)–(19). An equivalent formulation of the boundary value problem on the domain $\Omega = \Omega_1 \cup \Omega_2$ requires the validity of eq. (17) only in the sense of the L^2 inner product with an arbitrary test function v of a function space V, which leads to

$$\int_\Omega (-\nabla \cdot (c \nabla u) v + auv)\, d\mathbf{x} = 0 \quad \forall v \in V. \tag{20}$$

From the finite element analysis that is described in detail in Appendix A we derive a system of linear equations for the solution vector $U_{\Omega \setminus \Gamma_D}$ in the region $\Omega \setminus \Gamma_D$

$$(\mathbf{K} + \mathbf{M})\mathbf{U}_{\Omega \setminus \Gamma_\mathbf{D}} = -(\mathbf{K} + \mathbf{M})\mathbf{U}_{\Gamma_\mathbf{D}}. \tag{21}$$

$\mathbf{U}_{\Gamma_D}$ provides the non-zero Dirichlet boundary values on Γ_D.

To determine $\mathbf{U}_{\Omega \setminus \Gamma_D}$ from eq. (21) a direct solver of the Gauss elimination type is used. The computational effort to solve the system for approximately 250 000 degrees of freedom (d.o.f.) is about 40 s on a common personal computer (2.08 GHz, 2 GB RAM). We note that iterative methods are less expensive in terms of memory but they lack time efficiency. Since effective convergence requires an appropriate pre-conditioning of the system matrices, the desired solution of the discrete system of equations may not be achieved in reasonable computing time. Solving eq. (21) in connection with the adaptive mesh refinement based on an *a posteriori* error estimator as will be described in Sections 4.1 and 4.2 requires the solution of the system of equations in each refinement step which further reduces the efficiency of iterative solvers.

Our code is written in MATLAB®, from where the appropriate components are called. The finite element discretization is carried out using a MATLAB® toolbox for solving partial differential equations.

See Jin (1993) and Monk (2003) for further reading about FE applications in electromagnetics.

4.1 Error estimation

The quality of an FE solution can be remarkably improved by reducing the size of the grid elements. Unlike refining a mesh globally, an adaptive refinement strategy yields an optimal mesh with even less d.o.f.. The element-wise *a posteriori* error estimator

$$E^2(\vartheta) = \alpha \| - au^h \|^2 h_\vartheta^2 + \beta \frac{1}{2} \sum_{\tau \in \Gamma_{\text{int}}} \left\| - \mathbf{n}_\tau \cdot c \nabla u^h \right\|^2 h_\tau \tag{22}$$

based on the work of Johnson (1987) and Johnson & Erikson (1991) determines the regions for the adaptive mesh refinement. See Appendix B for a detailed derivation of eq. (22). The error indicator function depends on the local mesh size $h_\vartheta = h_\vartheta(\mathbf{x})$, the length h_τ of edge τ, the residual $-au^h$ on the triangle ϑ and the jump in the tangential electromagnetic fields $\mathbf{n}_\tau \cdot c \nabla u^h$ across the element edge τ that is distributed equally to both triangles sharing the edge by the factor $\frac{1}{2}$. By $\| \cdot \|$ the L_2-norm is denoted. The real coefficients α and β are independent of the triangulation. Note, that eq. (22) only contains known quantities including the approximate solution u^h. Hence, the error indicator can be computed without knowledge of the exact solution u.

4.2 Adaptive mesh refinement

On the basis of the error indicator function (22) an adaptive mesh refinement is carried out. Triangles for which $E^2(\vartheta)$ exceeds a certain value p relative to the largest estimated error are selected to be refined. Setting $p = 0.5$ means that all triangles with error indicator $E(\vartheta_i) > 0.5 \max[E(\vartheta)]$ are to be refined. Two main refinement schemes are applicable: (1) the longest-edge bisection creates two new triangles from an old one and (2) employing the regular refinement, four new triangles are generated from an old one by bisecting each edge. Usually, a combination of both is carried out to obtain meshes of high quality. Both schemes are suitable in the case of a global mesh refinement as well.

5 ACCURACY AND EFFICIENCY STUDIES

This section presents accuracy studies with analytical solutions that are available for the homogeneous and the 1-D layered half-space and comparisons of our code with other numerical results for the 2D-4 COMMEMI model. By comparison with analytical solutions we can quantify the numerical error arising from the FE

discretization. On the one hand, it depends on the mesh size and on the other hand it is imposed by non-exact boundary conditions.

For a fixed mesh, it is shown that the discretization error is mainly dependent on the electromagnetic skin depth, that is, on the electric conductivity and the frequency. By reducing the mesh size in certain regions of a homogeneous half-space it is illustrated how different adaptive mesh refinement strategies enhance the finite element solution.

Additionally, we have examined the influence of the air layer on the data at the earth's surface for E-polarization. For a simple dyke model, the exactness of the boundary conditions imposed at the upper horizontal domain boundary has proved to be dependent on the contrast in electric conductivity and on the thickness of the air layer.

5.1 Comparison with analytical solutions

Fig. 2 displays the apparent resistivity ρ_a, the phase angle ϕ and the error curves with reference to the analytic solutions on the surface of a homogeneous half-space of $\rho_1 = 10$ and $100\,\Omega$ m, respectively. The error levels indicate spatial grid patterns arising from the coarse initial mesh.

In the following, error specifications refer to the corresponding maximum levels.

For the $10\,\Omega$ m half-space the maximum error is more than 2 per cent for the apparent resistivity and 0.6° for the phase. In the case of the $100\,\Omega$ m half-space, however, the maximum errors are approximately 0.8 per cent and 0.2°, respectively. For a constant frequency of $f = 1$ Hz, the misfit to the analytical solution decreases with increasing skin depth $\delta \propto \sqrt{\rho}$. The same trend is pointed out by Fig. 3 that shows sounding curves of the apparent resistivity ρ_a and the phase ϕ for E- and H-polarization for the model of a $\rho_1 = 100\,\Omega$ m half-space with an embedded layer of $\rho_2 = 10\,\Omega$ m between $z_{\text{top}} = -200$ m and $z_{\text{bottom}} = -300$ m. The largest errors of approximately 13 per cent in apparent resistivity and 3° in phase for E-polarization and −17 per cent and −5° for H-polarization occur at the shortest period $T = 10^{-4}$ s and thus small skin depths. Note, that the error is almost negligible at the long period end ($T = 10^2$ s). Since the total number of grid nodes is limited by the available computer memory the maximum accuracy may be achieved by adapting the model size to T and ρ. Furthermore, to satisfy the boundary conditions the model requires horizontal and vertical extensions of several skin depths.

5.2 Accuracy enhancement strategies

Adaptive mesh refinement leads to an optimal trade-off between accuracy and computational effort. In the following, the results for the uniformly refined mesh used in the previous section (*cf.* Fig. 2b) are compared to those obtained by, first, a solely adaptive refinement and, secondly, a combination of both methods. We restrict our numerical investigations to the case of a $100\,\Omega$ m half-space.

For both strategies, values of the parameter p (*cf.* Section 4.2) have to be defined to select triangles for the adaptive mesh refinement. First, forcing the algorithm to restrict the refinement to triangles ϑ_i which show an estimated error of $E(\vartheta_i) > p \cdot \max(E(\vartheta))$, $p = 0.5$, results in a grid that is fine along the whole air–earth interface (*cf.* Fig. 4). Moreover, it gets remarkably coarser in the air layer but not towards greater depths.

Since computational resources are limited in terms of memory size, the number of d.o.f. is bounded. A redistribution of grid nodes according to an error indicator function avoids unnecessarily fine meshes in regions where the field usually shows small spatial variations. The second strategy incorporates an additional geometrical criterion that limits the adaption of the cell size to a certain area of interest which is determined by the skin depth, the location of lateral conductivity contrasts, and the centre of the model (Fig. 5). The choice of small p-values, for example, $p = 0.001$, ensures the very fine parametrization of the central part in spite of large estimated errors $E(\vartheta_i)$ outside of it. To prevent from numerical pollution effects of the coarse grid at the boundaries, a sequence of uniform refinement steps has to be performed until a limit for the number of mesh elements is exceeded.

The results of both strategies are displayed in Fig. 6. When applying an unrestricted adaptive mesh refinement, a moderate accuracy is obtained throughout the whole horizontal model extension (Fig. 6a). The combination of the adaptive and uniform mesh refinement (Fig. 6b) leads to very small errors of 0.2 per cent for the

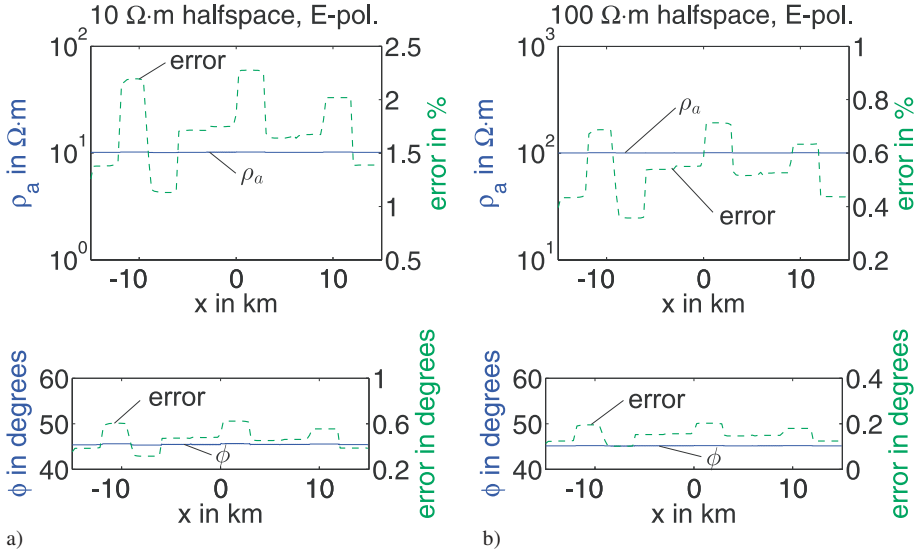

Figure 2. Apparent resistivity ρ_a (top, solid) and error in percent (top, dashed), phase angle ϕ (bottom, solid) and error in degrees (bottom, dashed) at the surface of (a) a $10\,\Omega$ m and (b) a $100\,\Omega$ m half-space at a frequency of $f = 1$ Hz, E-polarization, uniform mesh refinement, 219 777 d.o.f., 441 504 triangles.

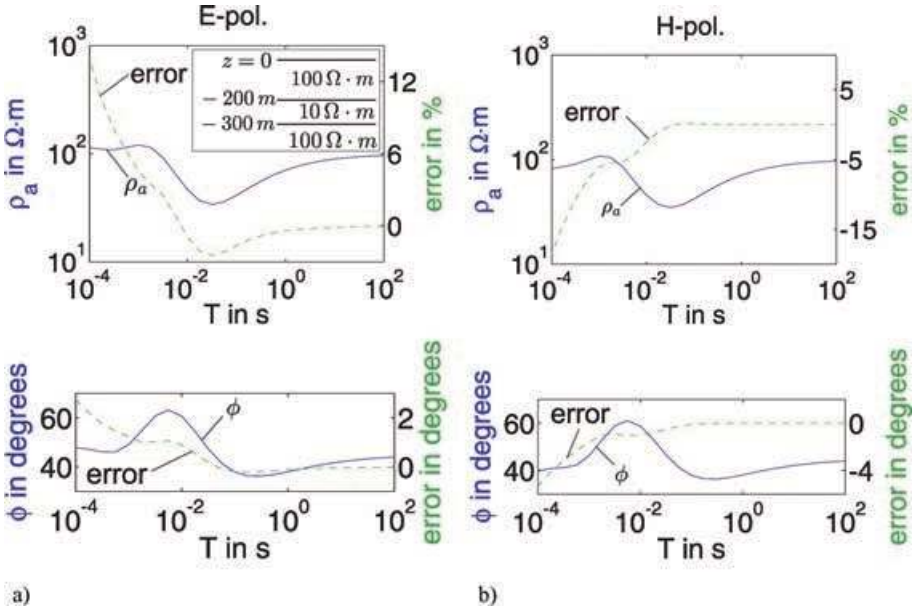

Figure 3. Soundings of apparent resistivity ρ_a (top, solid) and error in percent (top, dashed), phase angle ϕ (bottom, solid) and error in degrees (bottom, dashed) over a 100 Ω m half-space with an embedded 10 Ω m layer between −200 and −300 m depth, (a) E-polarization and (b) H-polarization, uniform mesh refinement, E-Pol.: 248 889 d.o.f., 499 456 triangles, H-Pol.: 279 345 d.o.f., 561 280 triangles.

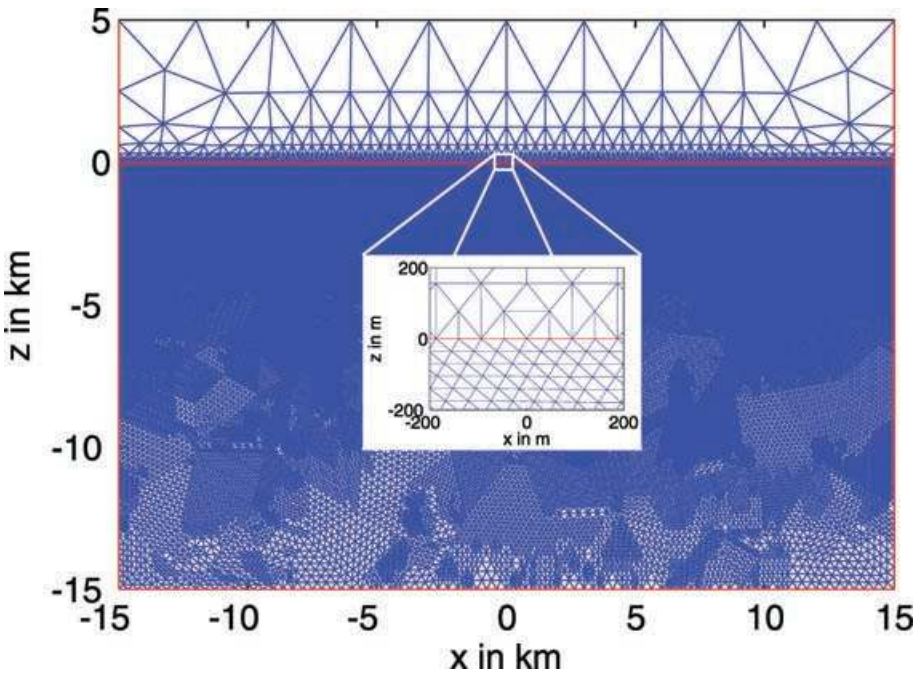

Figure 4. Adaptively refined mesh for an E-polarization model of a 100 Ω m half-space including the air layer. At the earth's surface, the minimum mesh size is $\Delta x_{\min} = 23.4$ m, the maximum $\Delta x_{\max} = 46.9$ m.

apparent resistivity and 0.05° for the phase in the central part of the model, which represents the area of interest.

Table 1 summarizes the comparison of the mesh refinement strategies in terms of accuracy and computational cost using a direct equation solver of the Gauss elimination type. Considering a desired error level of approximately 0.8 per cent in apparent resistivity and 0.2° in phase the combined adaptive and uniform mesh refinement appears as the most efficient method in terms of run time (10 s) and number of d.o.f. (37 793). Both other methods are slower by the factor five (50 s). In case of uniform mesh refinement the long run times are due to the large number of d.o.f. (219 777). In the other case, the solely adaptive refinement indeed leads to a reduced number of d.o.f. (86 596), however, the evaluation of the error indicator function (22) requires the numerical solution of the FE problem in every refinement step which thus leads to the undesirably long run times.

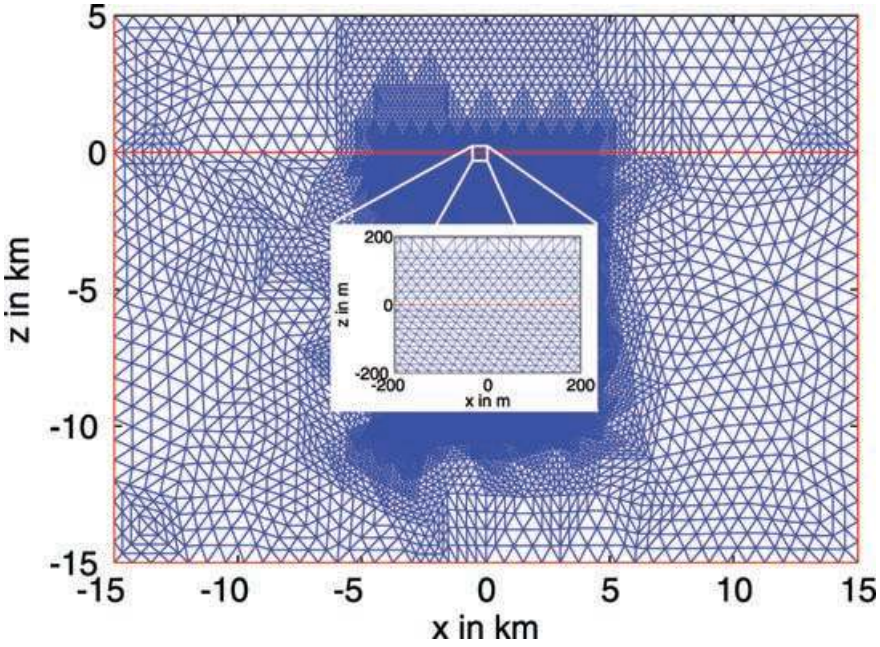

Figure 5. Adaptively and uniformly refined mesh for an E-polarization model of a 100 Ω m half-space including the air layer. At the earth's surface, the minimum mesh size is $\Delta x_{\min} = 23.4$ m, the maximum $\Delta x_{\max} = 750$ m.

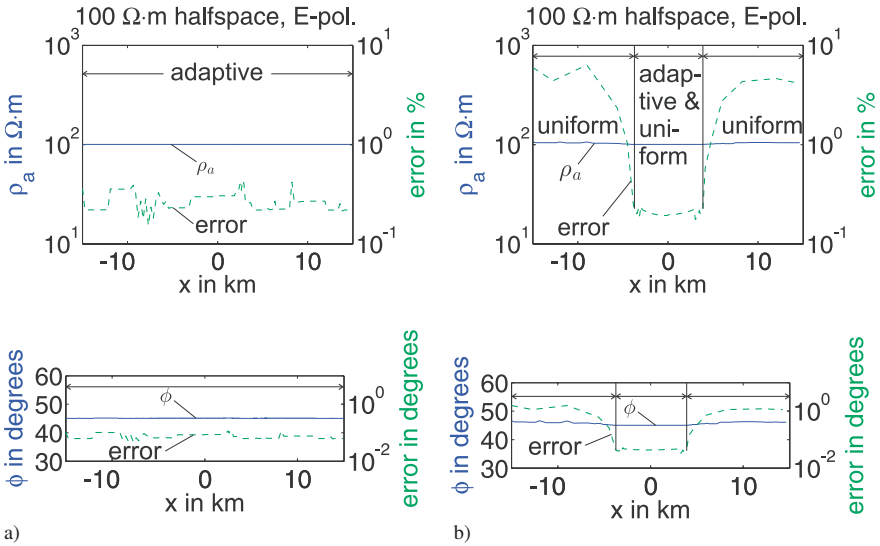

Figure 6. Apparent resistivity ρ_a (top, solid) and error in percent (top, dashed), phase angle ϕ (bottom, solid) and error in degrees (bottom, dashed) at the surface of a 100 Ω m half-space at a frequency of $f = 1$ Hz, E-polarization, (a) adaptive refinement: 174 746 d.o.f., 350 167 triangles, (b) combined adaptive and uniform refinement: 226 027 d.o.f., 452 208 triangles.

Table 1. Comparison of mesh refinement strategies with respect to accuracy and efficiency.

	Uniform	Adaptive	Adaptive & Uniform
d.o.f.	219 777	86 596	37 793
Number of triangles	441 504	173 873	75 722
Run time (s)	50	50	10
Error$_{\rho_a,\max}$ (per cent)	0.8	0.8	0.8
Error$_{\phi,\max}$ (°)	0.2	0.2	0.2

5.3 Influence of the air layer

Eqs (6) and (7) show that the magnetic field H_y is independent of the coordinates x and z within a non-conducting region. Hence, for H-polarization the inhomogeneous Dirichlet boundary condition assigns a constant H_y at the air–earth interface and the air layer need not be introduced explicitly as part of the model. By contrast, the real component of the electric field within the air is affected by subsurface changes of the conductivity. 2-D conductivity structures result in anomalous electric field contributions that attenuate in the air. Therefore, an air layer has to be introduced into the E-polarization models. The air layer can be regarded as sufficiently thick if these anomalous electric fields vanish at the upper horizontal model boundary and the field value approaches the one of the boundary condition due to the 1-D normal structure. Hence, the thickness of the air layer needs to be chosen with care in order to yield accurate results. As an example, we investigate two models consisting of a 100 Ω m half-space with an embedded vertical dyke

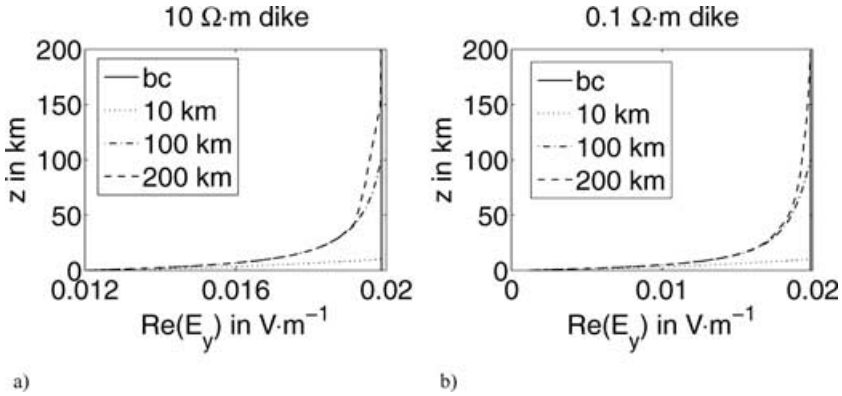

Figure 7. Real part of the electric field E_y in the air layer of a thickness of 10 km (dot), 100 km (dash–dotted) and 200 km (dash) for a 100 Ω m half-space with an embedded (a) 10 Ω m and (b) 0.1 Ω m dyke. The solid line indicates the boundary condition (bc) value. The asymptotic behaviour of the electric field is correct only for the 200 km thick air layer.

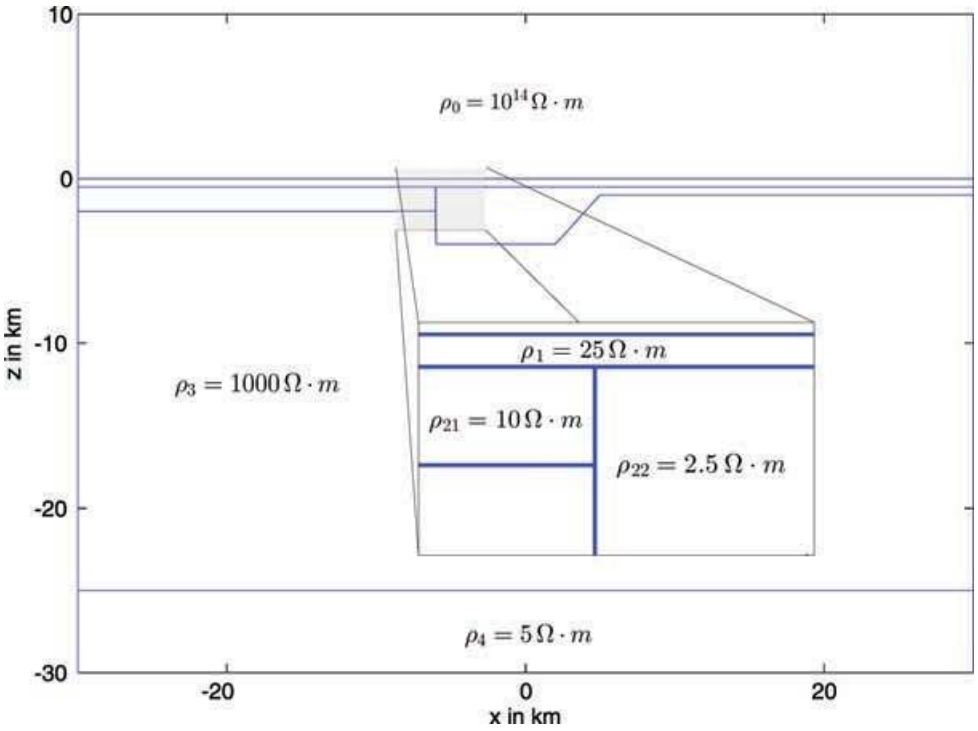

Figure 8. Section of the COMMEMI model 2D-4.

of 10 and 0.1 Ω m, respectively, at $-2000 \leq \times \leq 2000$ m for a frequency of $f = 1$ Hz. Fig. 7 displays vertical profiles of the real part of the electric field in the air layer at $x = 0$ m with respect to the air layer thickness (10, 100 and 200 km). The anomalous field contribution along a vertical profile in the air layer satisfies a radiation condition, hence, it yields a reduced total electric field that converges asymptotically to the boundary value. This behaviour is well represented in the case of the 200 km air layer. If the air layer is not sufficiently thick the graph shows a rather linear behaviour as for the thickness of 10 km. The effect on the real part of the electric field E_y is considerable up to $z = 150$ km for the 10 Ω m dyke and $z = 200$ km for the 0.1 Ω m dyke. The imaginary part of the electric field is unaffected by the thickness of the air layer.

The resulting distortion of the electric field E_y and its vertical gradient near the earth's surface leads to deviations of the apparent resistivity ρ_a of up to 1.5 per cent and of the phase ϕ of up to 1.2° in case of the 10 Ω m dyke. These values increase to 10 per cent and 2°, respectively, for the 0.1 Ω m dyke. Hence, the thickness of the air layer has to be determined by the magnitude of lateral conductivity contrasts.

5.4 Comparison with numerical calculations

One of the 2-D COMMEMI models (Weaver & Zhdanov 1997) serves as an example for comparing our FE approach with an FE program by Li (2000) and an FD code by Weaver (1986).

Fig. 8 displays the main features of the COMMEMI model 2D-4 which consists of three layers with resistivities $\rho_1 = 25\,\Omega$ m, $\rho_3 = 1000\,\Omega$ m and $\rho_4 = 5\,\Omega$ m. The embedded graben-like structure of $\rho_{22} = 2.5\,\Omega$ m tapers off as a layer to the right-hand model boundary. On the left-hand model boundary the stratification is different

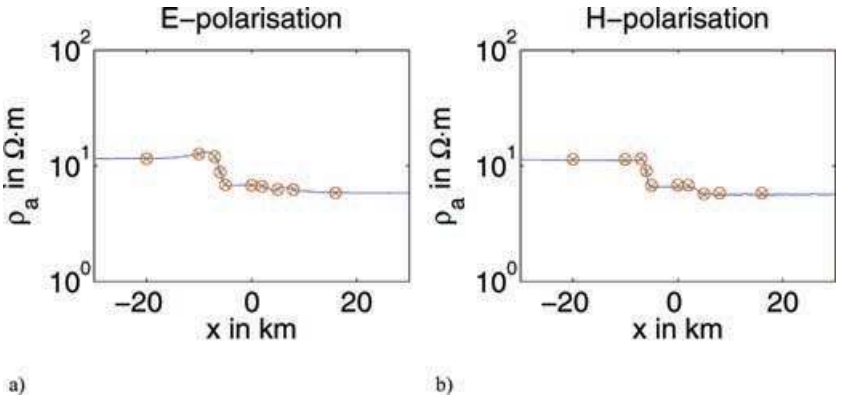

Figure 9. Apparent resistivitiy ρ_a computed with our FE code '−', by Li '×' and by Weaver '○' for the COMMEMI model 2D-4 of Fig. 8 at a frequency of $f = 1$ Hz for (a) E-polarization and (b) H-polarization. Deviations are below 1 per cent for E-polarization and below 3 per cent for H-polarization.

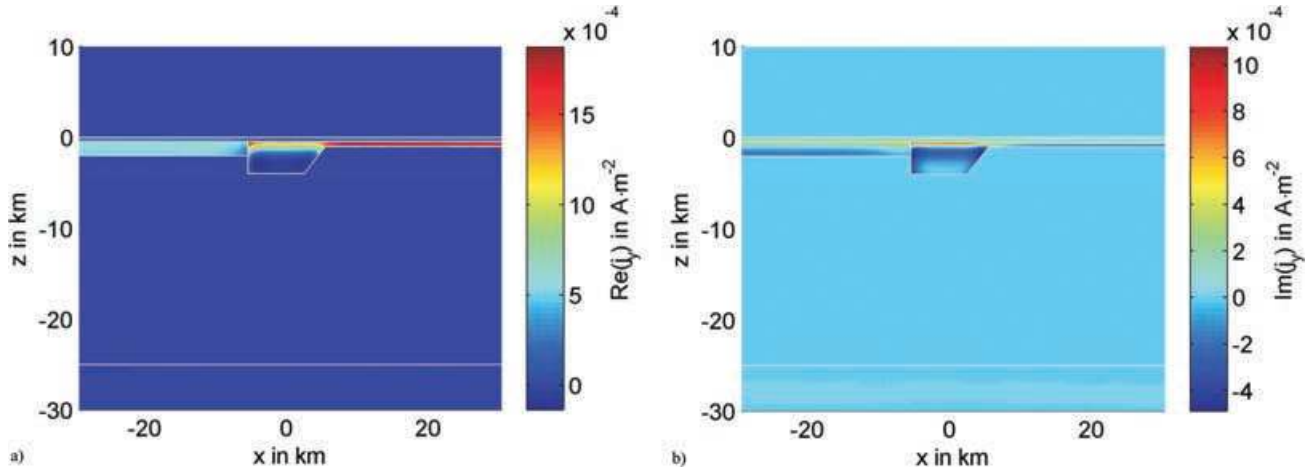

Figure 10. (a) Real and (b) imaginary part of current density j_y, $f = 1$ Hz, E-polarization.

because of a semi-infinite layer of $\rho_{21} = 10\,\Omega$ m. For our computations, the model extends to ± 30 km in the horizontal and to ± 50 km in the vertical direction. Inferred from the studies described in Section 5.3 we found an air layer of only 50 km to be sufficiently thick. This is caused by the overburden which significantly damps out the anomalous electric fields resulting from the lateral conductivity contrasts at $x = -6$ km.

The apparent resistivities computed by our algorithm and the two reference codes are shown in Fig. 9 for E- and H-polarization and a frequency of $f = 1$ Hz. With a maximum deviation below

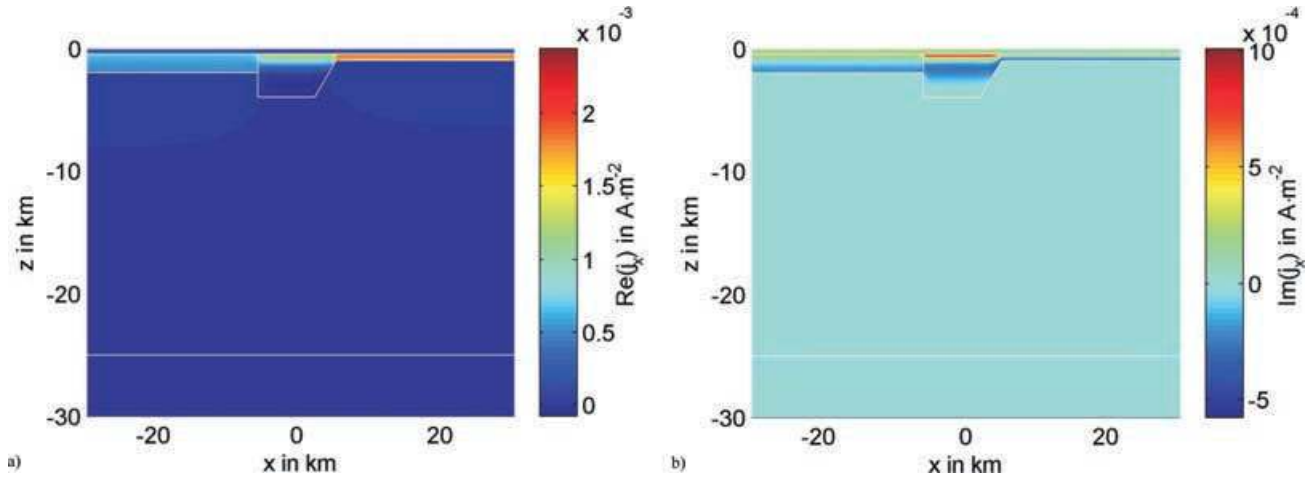

Figure 11. (a) Real and (b) imaginary part of current density j_x, f=1 Hz, H-polarization.

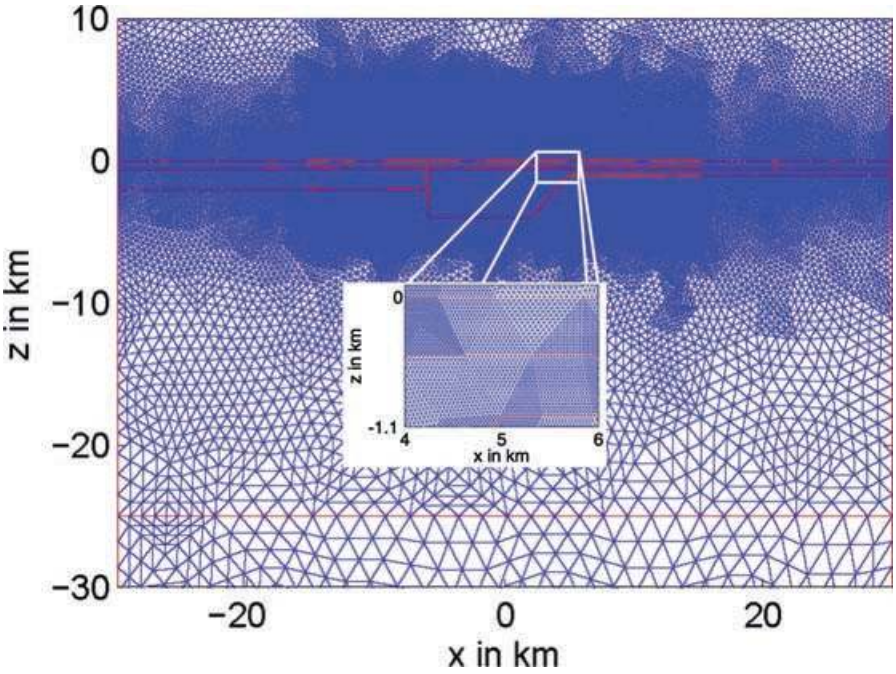

Figure 12. Section of the adaptively and uniformly refined mesh for the COMMEMI model 2D-4, E-polarization. Adaptive refinement has been restricted to $-15 < x < 15$ km and $-5 < z < 5$ km.

Table 2. Frequency f, resistivity ρ and skin depth δ for the models 'Land 1', 'Land 2' and 'Sea'.

	f (Hz)	ρ (Ω m)	δ (km)
Land 1	0.01	100 (crust)	50.3
Land 2	100	100 (crust)	0.5
Sea	0.01	1/3 (sea water), 100 (crust)	2.9, 50.3

1 per cent for E-polarization and below 3 per cent for H-polarization the results of the three codes are in good agreement.

Figs 10 and 11 present the horizontal current densities $j_y = \sigma E_y$ and $j_x = \sigma E_x$ for E- and H-polarization. In both cases, the currents focus in the upper conductive zones and decay with depth. Current channelling occurs within the thin 2.5 Ω m layer. Note that j_y is discontinuous at horizontal conductivity contrasts (Fig. 10) whereas j_x is continuous (Fig. 11). Large values of the imaginary parts of the current density j_y (Fig. 10b) and j_x (Fig. 11b) reflect strong induction effects in the conductive layers. The FE mesh applied for the E-polarization case is exemplified in Fig. 12. It has been generated by adaptive refinements starting from the initial grid for $-15 < x < 15$ km and $-5 < z < 5$ km and two subsequent uniform refinement steps. The mesh used for H-polarization is different as the air layer has been omitted.

6 MODEL STUDIES

The efficient and accurate modelling of a realistic air–earth interface whose shape may be derived, for example, by digital elevation models is feasible only by incorporating very fine triangular grids. They allow for treating natural slopes more flexibly than rectangular parametrizations. Triangular FE meshes that result from the decomposition of rectangular grid cells applied by Fox *et al.* (1980) and

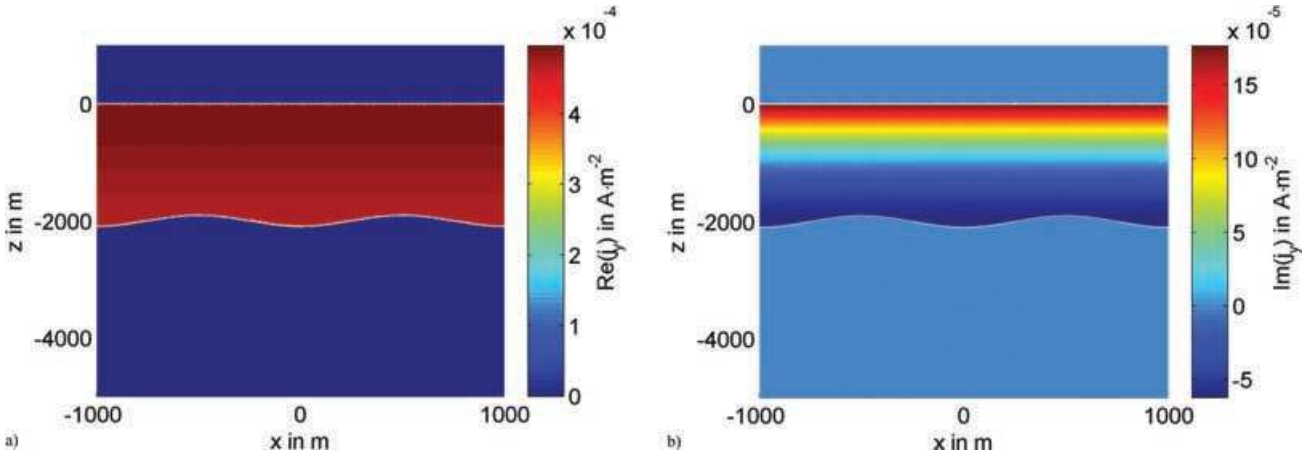

Figure 13. (a) Real and (b) imaginary part of current density j_y for E-polarization, model 'Sea': $\rho_0 = 10^{14}$ Ω m (air), $\rho_1 = 1/3$ Ω m (sea water), $\rho_2 = 100$ Ω m (crust), $f = 0.01$ Hz.

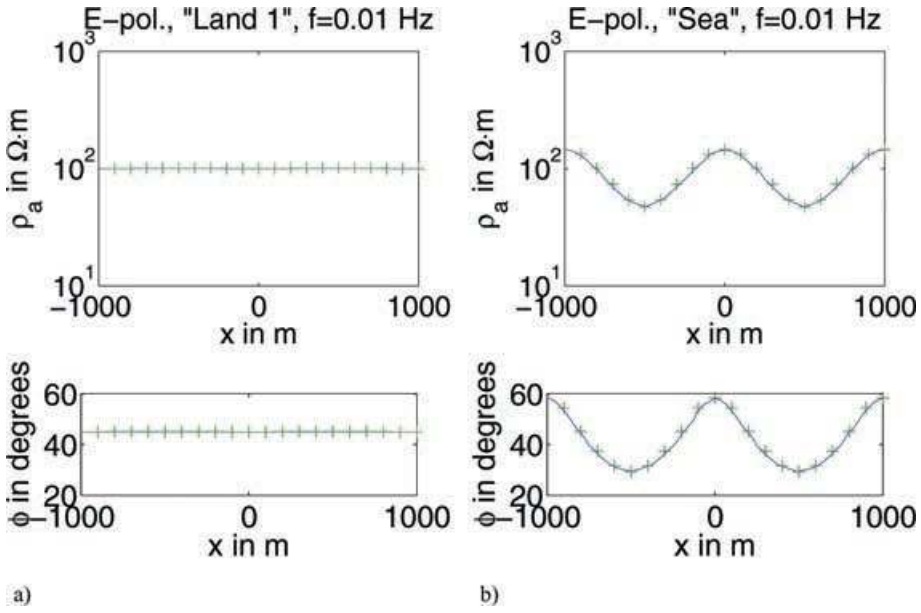

Figure 14. Apparent resistivity ρ_a (top) and phase ϕ (bottom) for a frequency of $f = 0.01$ Hz and models (a) 'Sea' and (b) 'Land 1', E-polarization, analytical '+' and numerical '−' solution.

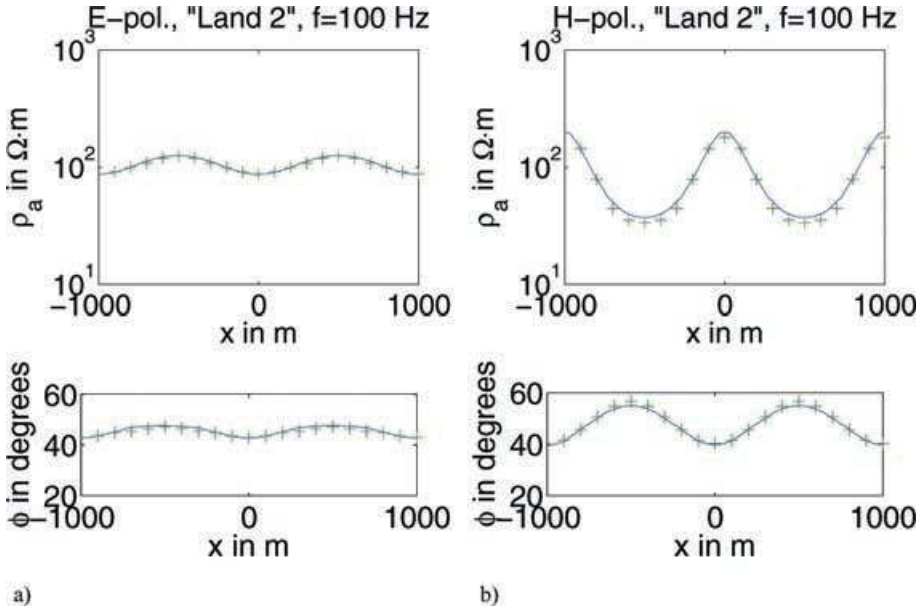

Figure 15. Apparent resistivity ρ_a (top) and phase ϕ (bottom) for the model 'Land 2', $f = 100$ Hz, (a) E-polarization and (b) H-polarization, analytical '+' and numerical '−' solution.

Wannamaker *et al.* (1986) are only suited for studying effects of a geometrically simple topography. Unstructured grids, however, provide a more precise discretization of arbitrary model geometries that can be used to include topographic or bathymetric data. To demonstrate the superiority of our unstructured grid based algorithm, we investigate two examples from the literature. The first one contains a sinusoidal surface which exhibits characteristic effects, whereas the second one is a close-to-reality example with real bathymetry data.

6.1 Synthetic example

With regard to the application of marine MT, Schwalenberg & Edwards (2004) introduced an analytical solution for a sinusoidal land surface and seafloor. Its shape is expressed as

$$z(x) = -\Delta \cos\left(\frac{2\pi}{\lambda}x\right) \tag{23}$$

with the amplitude $\Delta = 100$ m and the wave length $\lambda = 1000$ m. For the considered frequency range and resistivity values, the authors revealed very different topographic effects on the land surface and the seafloor. To discuss the effects of such a surface in different environments we investigate three special cases referred to as 'Land 1', 'Land 2' and 'Sea', respectively (see Table 2). Looking closer at the distribution of the current density $\mathbf{j} = \sigma\mathbf{E}$ we may gain a better physical understanding.

In the model 'Sea' we assume resistivities of $\rho_1 = \frac{1}{3}\,\Omega$ m for the sea water, $\rho_2 = 100\,\Omega$ m for the crust and a seafloor depth of

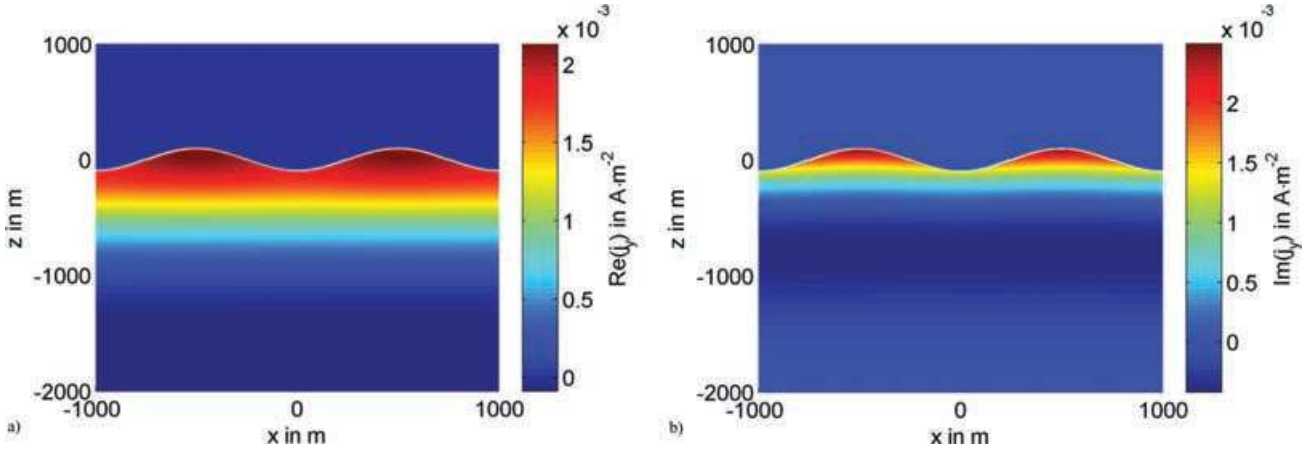

Figure 16. (a) Real and (b) imaginary part of the current density j_y for the model 'Land 2', $f = 100$ Hz, E-polarization.

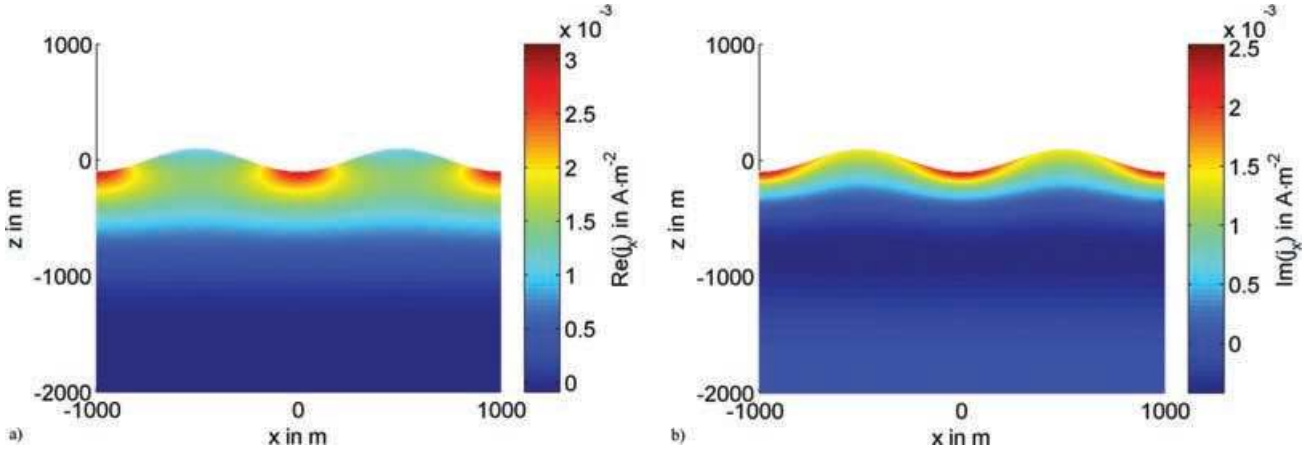

Figure 17. (a) Real and (b) imaginary part of current density j_x for the model 'Land 2', $f = 100$ Hz, H-polarization.

2000 m. Fig. 13 displays the current density component j_y for a frequency of 0.01 Hz and E-polarization. The currents mainly flow in the conductive sea water. The decay of the electromagnetic fields with depth (*cf.* the skin depth δ in Table 2) above the hills differs from the one in the valleys. This has significant influence on the apparent resistivity ρ_a and the phase ϕ displayed in Fig. 14(a). On land (model 'Land 1', Table 2), the undulations of the air–earth interface hardly affect the synthetic data (Fig. 14b) due to the large skin depth. The decay of the electromagnetic fields within 200 m from the top of the hills to the bottom of the valleys is negligible, that is, the skin depth is large compared to the amplitude of the seafloor undulations.

To cause topographic effects in the apparent resistivity ρ_a and the phase ϕ on land, the frequency has to be increased. Fig. 15 shows ρ_a and ϕ for E- and H-polarization and an adjusted frequency of $f = 100$ Hz (*cf.* Table 2, model 'Land 2').

In the case of E-polarization and higher frequency, the maximum values of apparent resistivity and phase are observed at the top of the hills, which is opposite to the observation made for the seafloor. We note that in the absence of the conducting sea water the crust acts as good conductor where the highest current densities occur at the hills (Fig. 16).

The current density component j_y caused by the sinusoidal shape of the earth's surface is larger on top of the hills than in the valleys. The lateral lack of current flow in the air results in a higher apparent resistivity and larger phase over the hills while the additional current flow near the valleys yields a decrease in the apparent resistivity and phase angle for E-polarization.

Considering currents flowing in-plane as is the case in H-polarization (Fig. 17), one observes large apparent resistivities and small phases in the valleys due to 'compressed' horizontal current lines and the associated horizontal magnetic and electric fields. On top of the hills the 'expansion' of the current lines gives rise to decreasing apparent resistivities and increased phases.

6.2 Real bathymetry model

We complete our numerical experiments with an example that demonstrates the capability of unstructured triangular grids to cope with real bathymetry data. We focus on the simulation of the effects caused by the strong seafloor topography at the East Pacific Rise at 17°S. In this region, the MELT experiment strives to map the distribution of rock melt at a mid-oceanic ridge (Evans *et al.* 1999). MT data have been collected at 13 ocean-bottom stations arranged perpendicular to the ridge strike (Fig. 18). Baba *et al.* (2006) recently published an interpretation based on a 2-D inversion incorporating anisotropy of the electrical conductivity. To account for the bathymetry, the MT responses have been corrected for 3-D topography as described by Baba & Chave (2005).

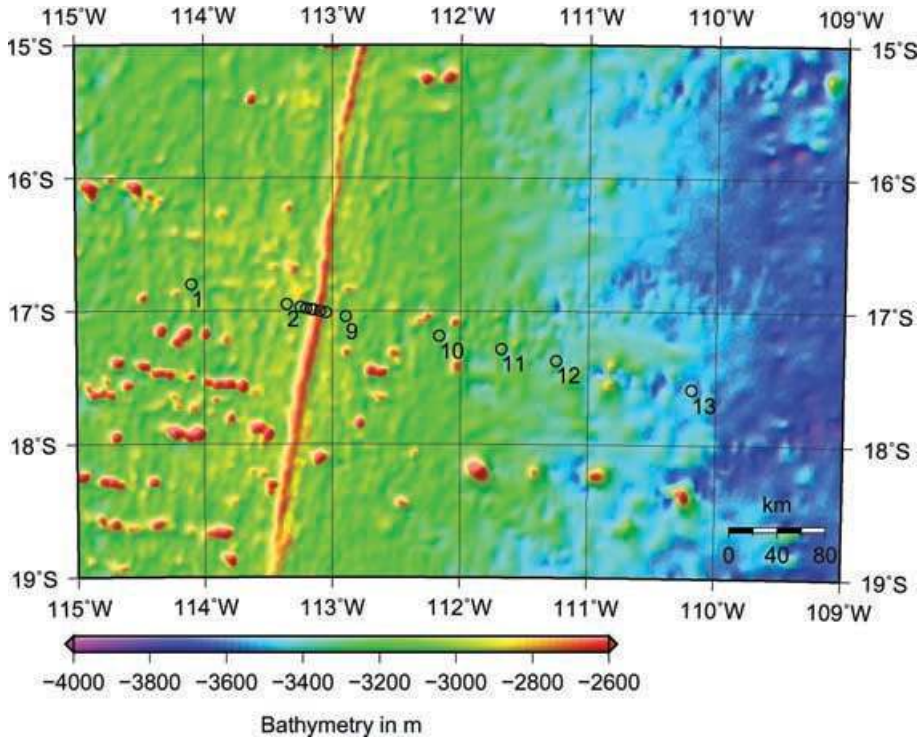

Figure 18. Location of MT sites (circles) on a bathymetric map.

Table 3. Bathymetry data of the data points on the profile across the mid-oceanic ridge.

No.	Dist. from ridge (km)	Depth (m)
1	−102.8	3346
2	−21.9	3084
3	−10.4	3167
4	−5.2	2817
5	−1.0	1636
6	1.0	2738
7	6.6	3022
8	11.2	3020
9	27.9	3126
10	107.7	3588
11	160.3	3538
12	206.8	3427
13	322.3	3610

Table 4. 1-D layered earth resistivity distribution for the mid-oceanic ridge model.

Depth (km)	Resistivity ρ (Ω m)
0 . . . 3.20	0.3125
3.20 . . . 9.39	1000
9.39 . . . 51.49	5000
51.49 . . . 393.29	50
>393.29	1

In the following, we show to what extent apparent resistivity and phase are affected by the seafloor topography of this region for a considered period range of $10^2 < T < 10^5$ s. For this purpose, we combine the bathymetry data listed in Table 3 and the 1-D layered earth model in Table 4 used for the terrain correction by Baba *et al.* (2006). We assume a 2-D representation of the topography to be sufficient since the rise as the main bathymetric feature can be regarded as a 2-D structure. Fig. 19 displays the results as pseudo-sections for E- and H-polarization, respectively. In the case of E-polarization, we observe decreased apparent resistivities and increased phases at the rise (sites 4–7) as well as enlarged apparent resistivities and diminished phases at depressions (sites 3, 8, 9, 11 and 12). These observations coincide with the results of the previous section. We note that sites 3 and 8 exhibit phases larger than 90°. Due to the concentration of the currents in the sea water at the slope, the anomalous magnetic field dominates the strongly attenuated normal field at the seafloor. The anomalous field is opposite in sign and yields phases that lie in the second quadrant. For the H-polarization case, the bathymetry effect is caused by a static, frequency-independent accumulation of electric charge at horizontal conductivity contrasts. At the rise, the amplification of the electric field yields a maximum apparent resistivity, whereas at the depressions the electric field is diminished and the apparent resistivity decreases. The phase is less affected by the electric charge accumulation.

Fig. 20 shows the unstructured triangular grid that has been used in the FE simulation of the electric field for E-polarization at the period of $T = 10^2$ s. The mesh used for the H-polarization differs from the latter as the air layer has been omitted. Both meshes result from adaptive mesh refinement. The triangular elements are generally fine in the layer representing the sea and in the upper crust where most of the electric field is attenuated. The seafloor undulations are parametrized very finely. In the deeper crust where the field values are close to zero the grid is coarse. The dense coverage of grid cells constricted to regions where the solution requires a good resolution guarantees a precise parametrization of the bathymetric undulations as well as accurate and reliable results.

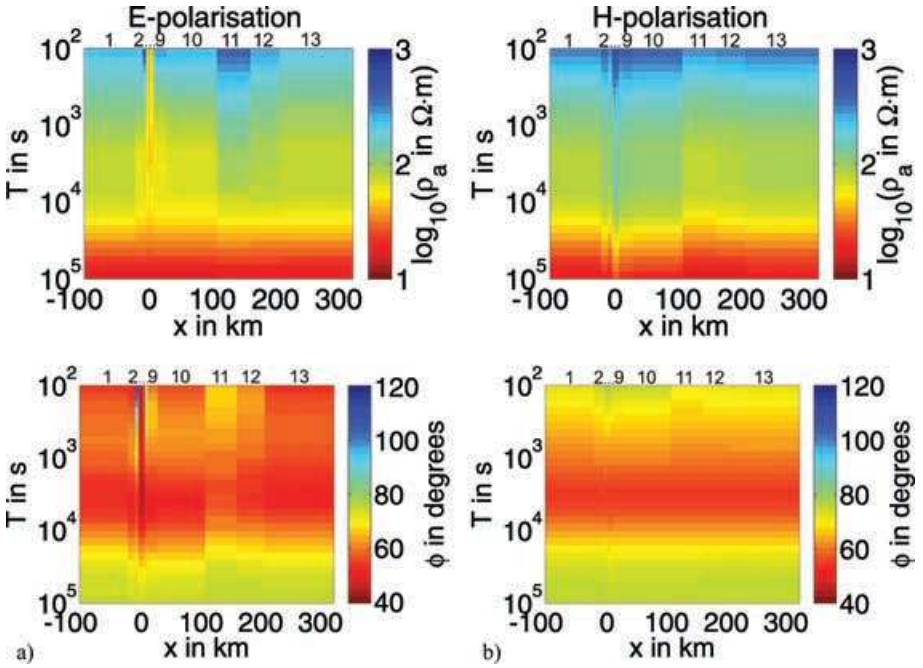

Figure 19. Pseudo-sections of apparent resistivity ρ_a (top) and phase ϕ (bottom) for the mid-oceanic ridge model for (a) E-polarization and (b) H-polarization. Numbers at the top denote MT sites plotted in Fig. 18.

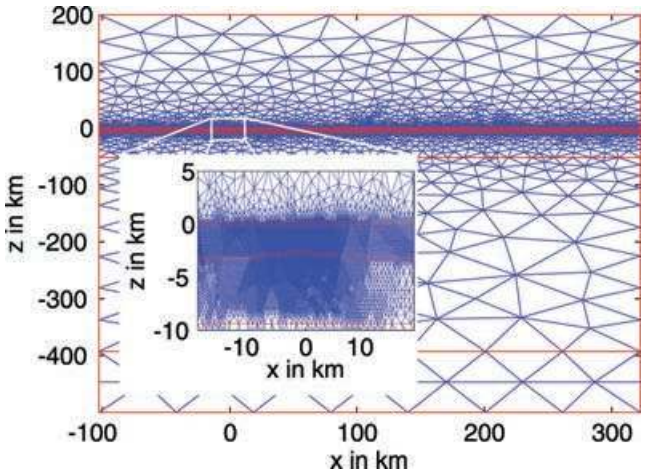

Figure 20. FE mesh parametrizing the model of the mid-oceanic ridge, $f = 0.01$ Hz, E-polarization.

7 CONCLUSIONS

We have developed an FE approach for modelling plane-wave diffusive time-harmonic electromagnetic fields. The appropriate boundary value problem can be expressed as an elliptical second-order partial differential equation including inhomogeneous Dirichlet boundary conditions arising from a 1-D layered half-space. A system of linear equations results from applying the FE approximation with linear basis functions on unstructured triangular grids. For the considered 2-D problems, direct methods on the basis of classical Gauss type equation solvers are sufficient to obtain the solutions in reasonable time.

The comparison with analytical solutions and numerical calculations has shown that our FE approach is numerically robust. *A posteriori* error estimators are the basis for an adaptive mesh generation that guarantees high accuracy. A combined adaptive and uniform mesh refinement strategy yields an optimum trade-off between accuracy and computational effort.

The use of unstructured grids is very suitable for simulating electromagnetic fields in arbitrary model geometries especially when surface topography is involved. Model studies have shown, that undulations of the earth's surface significantly affect the apparent resistivity and phase depending on different skin depths on land and in the sea. Considering the mid-oceanic ridge model including real bathymetry data, it becomes obvious to what extent seafloor undulations can influence MT measurements. Hence, it is of great importance to allow for modelling of any topographic shape.

The utilization of MATLAB®'s pde-toolbox has greatly simplified our approach to simulate electromagnetic fields in complicated geological environments. High-level programming languages are very suitable to takeover tedious administration tasks as is the case for FE modelling. This leaves more space to deal with the actual physical phenomena. However, we find it of prime importance to pervade the theoretical background and control the implementation of the numerical techniques. Serving as a fast and accurate forward code it is well suited to be integrated in an inversion scheme accounting for topography. This will be the subject of a forthcoming publication.

ACKNOWLEDGMENTS

We thank Katrin Schwalenberg for providing her code for the analytic computation of the electromagnetic fields on a sinusoidal land surface and seafloor. Thanks go to the SEG for supporting AF by the Gerald W. Hohmann graduate scholarship. We acknowledge the suggestions by Yuguo Li and two anonymous reviewers for improving the manuscript.

REFERENCES

Aprea, C., Booker, J.R. & Smith, J.T., 1997. The forward problem of electromagnetic induction: accurate finite-difference approximations for two-dimensional discrete boundaries with arbitrary geometry, *Geophys. J. Int.,* **129,** 29–40.

Baba, K. & Chave, A.D., 2005. Correction of seafloor magnetotelluric data for topographic effects during inversion, *J. geophys. Res.,* **110,** B12105, doi:10.1029/2004JB003463.

Baba, K., Chave, A.D., Evans, R.L., Hirth, G. & Mackie, R.L., 2006. Mantle dynamics beneath the East Pacific Rise at 17°S: insights from the Mantle Electromagnetic and Tomography (MELT) experiment, *J. geophys. Res.,* **111,** B02101,doi:10.1029/2004JB003598.

Baba, K. & Seama, N., 2002. A new technique for the incorporation of seafloor topography in electromagnetic modelling, *Geophys. J. Int.,* **150,** 392–402.

Brewitt-Taylor, C.R. & Weaver, J.T., 1976. On the finite difference solution of two-dimensional induction problems, *Geophys. J. R. astr. Soc.,* **47,** 375–396.

Chouteau, M. & Bouchard, K., 1988. Two-dimensional terrain correction in magnetotelluric surveys, *Geophysics,* **53,** 854–862.

Coggon, J.H., 1971. Electromagnetic and electrical modeling by the finite element method, *Geophysics,* **36,** 132–155.

Evans, R.L. *et al.*, 1999. Asymmetric electrical structure in the mantle beneath the East Pacific Ridge at 17°S, *Science,* **286,** 752–756.

Fox, R.C., Hohmann, G.W., Killpack, T.J. & Rijo, L., 1980. Topographic effects in resistivity and induced-polarization surveys, *Geophysics,* **45,** 75–93.

Franke, A., Börner, R.-U. & Spitzer, K., 2004. 2-D Finite Element modelling of plane-wave diffusive time-harmonic electromagnetic fields using adaptive unstructured grids, *Proceedings of IAGA WG 1.2 Workshop on Electromagnetic Induction in the Earth,* October 18–23, 2004, Hyderabad, India, S2-O01, 1–4. WWW-document, http://emindia2004.org/abstracts.htm.

Hohmann, G.W., 1971. Electromagnetic scattering by conductors in the earth near a line source of current, *Geophysics,* **36,** 101–131.

Hohmann, G.W., 1975. Three-dimensional induced polarization and electromagnetic modeling, *Geophysics,* **40,** 309–324.

Holland, R., 1993. Pitfalls of staircase meshing, *IEEE Trans. Electromagnet. Compat.,* **35 (4),** 434–439.

Jin, J., 1993. *The Finite Element Method in Electromagnetics,* John Wiley & Sons, Inc., New York, USA.

Jiracek, G.R., Reddig, R.P. & Kojima, R.K., 1989. Application of the Rayleigh-FFT to magnetotelluric modeling and correction, *Phys. Earth planet. Inter.,* **53,** 365–375.

Johnson, C., 1987. *Numerical Solution of Partial Differential Equations by the Finite Element Method* Studentlitteratur, Lund, Schweden.

Johnson, C. & Erikson, K., 1991. Finite element methods for parabolic problems I: a linear model problem, *SIAM J. Numer. Anal.,* **28,** 43–77.

Jones, F.W. & Pascoe, L.J., 1971. A general computer program to determine the perturbation of alternating electric currents in a two-dimensional model of a region of uniform conductivity with an embedded inhomogeneity, *Geophys. J. R. astr. Soc.,* **24,** 3–30.

Jones, F.W. & Price, A.T. 1970. The perturbations of alternating geomagnetic fields by conductivity anomalies. *Geophys. J. R. astr. Soc.,* **20,** 317–334.

Li, Y., 2000. Numerische Modellierungen von elektromagnetischen Feldern in 2- und 3-dimensionalen anisotropen Leitfähigkeitsstrukturen der Erde nach der Methode der Finiten Elemente, *PhD thesis*, Universität Göttingen, Cuvillier Verlag Göttingen.

Mackie, R.L., Madden, T.R. & Wannamaker,, P., 1993. Three-dimensional magnetotelluric modeling using difference equations—theory and comparisons to integral equation solutions. *Geophysics,* **58,** 215–226.

McFee, S. & Giannacopoulos, D., 2001. Optimal discretizations in adaptive finite element electromagnetics, *Int. J. Numer. Methods Eng.,* **52(9)**, 939–978.

Mitsuhata, Y. & Uchida, T., 2004. 3D magnetotelluric modeling using the T-Ω finite-element method, *Geophysics,* **69,** 108–119.

Monk, P., 2003. *Finite Element Methods for Maxwell's Equations,* Oxford University Press Inc., New York.

Raiche, A.P., 1974. An integral equation approach to three-dimensional modelling, *Geophys. J. R. astr. Soc.,* **36,** 363–376.

Reddy, I.K. & Rankin, D., 1975. Magnetotelluric response of laterally inhomogeneous and anisotropic media, *Geophysics,* **40(6)**, 1035–1045.

Schwalenberg, K. & Edwards, R.N., 2004. The effect of seafloor topography on magnetotelluric fields: an analytical formulation confirmed with numerical results, *Geophys. J. Int.,* **159,** 607–621.

Wait, J.R., 1953. Propagation of radio waves over a stratified ground. *Geophysics,* **20,** 416–422.

Wannamaker, P.E., Hohmann, G.W. & SanFilipo, W.A., 1984. Electromagnetic modeling of three-dimensional bodies in layered earths using integral equations, *Geophysics,* **49,** 60–74.

Wannamaker, P.E., Stodt, J. & Rijo, L., 1986. Two-dimensional topographic responses in magnetotellurics modeled using finite elements, *Geophysics,* **51,** 2131–2144.

Wannamaker, P.E., Stodt, J.A. & Rijo, L., 1987. A stable finite element solution for two-dimensional magnetotelluric modelling, *Geophys. J. R. astr. Soc.,* **88,** 277–296.

Weaver, J.T., 1986. *Finite difference calculations for COMMEMI,* Department of Physics, University Victoria.

Weaver, J.T., 1994. *Mathematical Methods for Geo-Electromagnetic Induction,* Research Studies Press Ltd., John Wiley & Sons, Inc., New York, USA.

Weaver, J.T. & Zhdanov, M.S., 1997. Methods for modelling electromagnetic fields, *J. Appl. Geophys.,* **37,** 133–271.

Webb, J.P., 1995. Application of the finite-element method to electromagnetic and electrical topics, *Rep. Prog. Phys.,* **58(12)**, 1673–1712.

Weidelt, P., 1975. Electromagnetic induction in three-dimensional structures, *J. Geophys.,* **41,** 85–109.

APPENDIX A: FINITE ELEMENT FORMULATION

We seek for a solution u of the boundary value problem described by eqs (17)–(19). An equivalent formulation of the boundary value problem on the domain $\Omega = \Omega_1 \cup \Omega_2$ requires the validity of eq. (17) only in the sense of the L^2 inner product with an arbitrary test function v of a function space V, which leads to

$$\int_\Omega (-\nabla \cdot (c\nabla u)v + auv)\, d\mathbf{x} = 0 \quad \forall v \in V. \tag{A1}$$

From the vector identity $\nabla \cdot (c\nabla uv) = \nabla \cdot (c\nabla u)v + c\nabla u \cdot \nabla v$ and Green's Theorem we obtain

$$\int_\Omega (c\nabla u \cdot \nabla v + auv)\, d\mathbf{x} - \int_{\partial\Omega} \mathbf{n} \cdot (c\nabla u)v\, dl = 0 \quad \forall v \in V. \tag{A2}$$

The integral over all boundaries $\partial\Omega = \Gamma_D \cup \Gamma_{\text{int}}$ of the region Ω

$$\int_{\partial\Omega} \mathbf{n} \cdot (c\nabla u)v\, dl = \int_{\Gamma_D} \mathbf{n} \cdot (c\nabla u)v\, dl + \int_{\Gamma_{\text{int}}} [\mathbf{n}_1 \cdot (c_1\nabla u_1) + \mathbf{n}_2 \cdot (c_2\nabla u_2)]v\, dl \tag{A3}$$

vanishes if $v \equiv 0$ on the Dirichlet boundary Γ_D. On that condition, the original problem (17)–(19) can be replaced by the so-called weak formulation which consists of finding $u \in U$ such that:

$$b(u, v) = \int_\Omega (c\nabla u \cdot \nabla v + auv)\, d\mathbf{x} = 0 \quad \forall v \in V, \tag{A4}$$

where

$$U := \{u \in H^1(\Omega) : u = r \quad \text{on} \quad \Gamma_D\} \quad \text{and} \tag{A5}$$

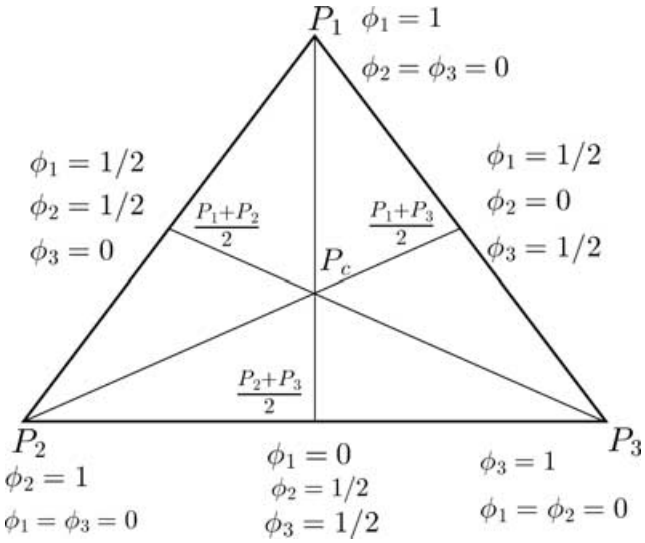

Figure A1. Linear basis functions $\phi_m^\vartheta(P_n)$ $(m, n = 1, 2, 3)$ on triangle t, $\phi_m^\vartheta(P_n) = 1$ $(m = n)$ and $\phi_m^\vartheta(P_n) = 0$ $(m \neq n)$.

$$V := \{v \in H^1(\Omega) : v \equiv 0 \quad \text{on} \quad \Gamma_D\} \tag{A6}$$

are the trial and the test space, respectively. H^1 denotes the finite-dimensional Hilbert space

$$H^1(\Omega) := \{v \in L^2(\Omega), \nabla v \in [L^2(\Omega)]^2\}, \tag{A7}$$

that is, linear with respect to the scalar product $(u, v) = \int_\Omega (uv + \nabla u \cdot \nabla v)\, d\mathbf{x}$. For the solution u of the weak form (A4) and its first partial derivatives ∇u it is sufficient to be square integrable instead of $u \in C^2(\Omega_1, \Omega_2)$ (*cf.* eq. 17). The material parameters $a, c \in L^2(\Omega)$ are required to be square integrable. Satisfying eqs (17)–(19), the electromagnetic fields are solutions to eq. (A4) as well.

Subsequently, we seek a discrete formulation of eq. (A4). Preliminary, the solution u and the test function v are both required to belong to the same infinite-dimensional function space V, that is, $r \equiv 0$ in eq. (A5). The inhomogeneous Dirichlet boundary conditions $u = r \not\equiv 0$ will be taken into account later. Projection of the weak form onto an N_p-dimensional function subspace V_{N_p} means requiring $u, v \in V_{N_p}$. Taking N_p test functions $\phi_i \in V_{N_p}$ that form a basis of V_{N_p} and u^h as a linear combination of these basis functions and the scalar complex expansion coefficients U_j

$$u^h(\mathbf{x}) = \sum_{j=1}^{N_p} U_j \phi_j(\mathbf{x}) \tag{A8}$$

we obtain the system of equations

$$\sum_{j=1}^{N_p} \left(\int_\Omega ((c\nabla\phi_j) \cdot \nabla\phi_i + a\phi_j\phi_i) d\mathbf{x} \right) U_j = 0, \quad i = 1, \ldots, N_p. \tag{A9}$$

It can be rewritten in matrix form

$$(\mathbf{K} + \mathbf{M})\mathbf{U} = \mathbf{0}, \tag{A10}$$

with the stiffness matrix

$$K_{i,j} = \int_\Omega (c\nabla\phi_j) \cdot \nabla\phi_i d\mathbf{x} \quad i, j = 1, \ldots, N_p \tag{A11}$$

and the mass matrix

$$M_{i,j} = \int_\Omega a\phi_j\phi_i d\mathbf{x} \quad i, j = 1, \ldots, N_p. \tag{A12}$$

We simply choose V_{N_p} to be a space of piecewise linear functions. Linear Lagrange elements are well suited for simulating scalar field components in source-free regions, for example, in the 2-D MT case. In the 3-D case, however, the application of curl-conforming vector elements seems to be more natural due to the conditions of continuity of the electromagnetic vector fields. Using $\phi_i(\mathbf{x_i}) = 1$ in eq. (A8) leads to

$$u^h(\mathbf{x_i}) = \sum_{j=1}^{N_p} U_j \phi_j(\mathbf{x_i}) = U_i. \tag{A13}$$

Hence, solving eq. (A10) yields the nodal values of the approximate solution $u^h(\mathbf{x})$.

The system matrices $\mathbf{K}$ and $\mathbf{M}$ are assembled from the local matrices $\mathbf{K}^\vartheta$ and $\mathbf{M}^\vartheta$, respectively, of each triangle ϑ. The integrals in eqs (A11) and (A12) are computed by the midpoint rule:

$$K_{m,n}^\vartheta = c(P_c)\frac{1}{4A^\vartheta} \begin{pmatrix} \beta_n \\ \alpha_n \end{pmatrix}^T \begin{pmatrix} \beta_m \\ \alpha_m \end{pmatrix}, \quad m, n = 1, 2, 3, \tag{A14}$$

$$M_{m,n}^\vartheta = a(P_c)\frac{A^\vartheta}{12}(1 + \delta_{m,n}), \quad m, n = 1, 2, 3, \tag{A15}$$

where

$$\begin{aligned} \alpha_1 &= x_3 - x_2, \quad & \beta_1 &= z_2 - z_3, \\ \alpha_2 &= x_1 - x_3, \quad & \beta_2 &= z_3 - z_1, \\ \alpha_3 &= x_2 - x_1, \quad & \beta_3 &= z_1 - z_2. \end{aligned} \tag{A16}$$

The coefficients a and c are assigned to the centre of mass P_c of the triangle. A^ϑ denotes the area of triangle ϑ and $\delta_{m,n}$ the Kronecker delta. m, n are the local numbering indices. To illustrate the quadrature formulas, Fig. A1 displays the triangle ϑ and the basis functions ϕ_m^ϑ. Every element of the local matrices $K_{m,n}^\vartheta$ and $M_{m,n}^\vartheta$ is added to the appropriate element of the system matrices $K_{i,j}$ and $M_{i,j}$, respectively, taking into account the relationship between local and global numbering of the grid nodes.

The inhomogeneous Dirichlet boundary conditions with $r \not\equiv 0$ still need consideration. So far, the vector $\mathbf{U}$ contains N_p elements for the interior points in region $\Omega \setminus \Gamma_D$ and N_{Γ_D} elements for the points on Γ_D whose values vanish (*cf.* eq. A6). Eq. (18) provides the N_{Γ_D} non-zero values on Γ_D in $\mathbf{U}_{\Gamma_D}$ which comprises N_p zero-elements for all the interior points. Applying

$$\mathbf{U} = \mathbf{U}_{\Omega\setminus\Gamma_D} + \mathbf{U}_{\Gamma_D} \tag{A17}$$

to eq. (A10), we derive a system of linear equations for $\mathbf{U}_{\Omega\setminus\Gamma_D}$:

$$(\mathbf{K} + \mathbf{M})\mathbf{U}_{\Omega\setminus\Gamma_\mathbf{D}} = -(\mathbf{K} + \mathbf{M})\mathbf{U}_{\Gamma_\mathbf{D}}. \tag{A18}$$

APPENDIX B: ERROR INDICATOR FUNCTION

The error $e^h = u - u^h$ of the FE approximation satisfies the variational formulation

$$b(e^h, v) = b(u, v) - b(u^h, v) = -b(u^h, v) = R^h(v) \quad \forall v \in V, \tag{B1}$$

where R^h is called the weak residual. According to eq. (A4), eq. (B1) can be rewritten as

$$b(e^h, v) = -\int_\Omega (c\nabla u^h \cdot \nabla v + a u^h v)\, d\mathbf{x} \quad \forall v \in V. \tag{B2}$$

Splitting the domain integral into contributions of each element ϑ yields

$$b(e^h, v) = \sum_{\vartheta \in \Omega} \left(- \int_{\vartheta} (c \nabla u^h \cdot \nabla v + a u^h v) \, d\mathbf{x} \right) \quad \forall v \in V. \tag{B3}$$

The vector identity $\nabla \cdot (c \nabla u v) = \nabla \cdot (c \nabla u) v + (c \nabla u) \cdot \nabla v$ and Green's Theorem lead to

$$b(e^h, v) = \sum_{\vartheta \in \Omega} \int_{\vartheta} (\nabla \cdot (c \nabla u^h) - a u^h) v \, d\mathbf{x} - \sum_{\tau \in \Gamma_{\text{int}}} \int_{\tau} \mathbf{n}_\tau c \nabla u^h v \, dl \quad \forall v \in V, \tag{B4}$$

where $\tau \in \Gamma_{\text{int}}$ includes all interior edges on the domain Ω. For the exterior boundaries $v \equiv 0$ holds (*cf.* eq. A6). Since the basis functions are linear, the term $\nabla \cdot (c \nabla u^h)$ vanishes. According to interpolation theory (Johnson 1987), the error that arises from projecting $v \in V$ to $v^h \in V_{N_p}$ can be estimated as $\nu_1 h_\vartheta \|v\|$ on all triangles ϑ and $\nu_2 \sqrt{h_\tau} \|v\|$ on all edges τ with $\nu_1, \nu_2 \in R$ being constant for a triangulation. h_ϑ and h_τ denote the local mesh size and the length of edge τ, respectively. A typical measure for the local mesh size h_ϑ is the circumradius of the triangle ϑ. Using these estimates and the Cauchy-Schwarz inequality we derive

$$b(e^h, v) \leq \|v\| \times \left(\nu_1 \sum_{\vartheta \in \Omega} \| - a u^h \|^2 h_\vartheta^2 + \nu_2 \sum_{\tau \in \Gamma_{\text{int}}} \| - \mathbf{n}_\tau c \nabla u^h \|^2 h_\tau \right)^{1/2} \quad \forall v \in V. \tag{B5}$$

Employing the inequality $\kappa \|v\|^2 \leq b(v, v) (\kappa \in R, \kappa = \text{const.})$ and substituting e^h in place of v an element-wise local error indicator $E(\vartheta)$ can be obtained

$$\|e^h\|^2 \leq E^2(\vartheta) = \alpha \| - a u^h \|^2 h_\vartheta^2 + \beta \frac{1}{2} \sum_{\tau \in \Gamma_{\text{int}}} \| - \mathbf{n}_\tau \cdot c \nabla u^h \|^2 h_\tau, \tag{B6}$$

where $\alpha = \nu_1^2 / \kappa^2$ and $\beta = \nu_2^2 / \kappa^2$. The error indicator function depends on the local mesh size $h_\vartheta = h_\vartheta(\mathbf{x})$, the length h_τ of edge τ, the residual $-a u^h$ on the triangle ϑ and the jump in the tangential electromagnetic fields $\mathbf{n}_\tau \cdot c \nabla u^h$ across the element edge τ that is distributed equally to both triangles sharing the edge by the factor $\frac{1}{2}$. By $\| \cdot \|$ the L_2-norm is denoted. The real coefficients α, β, ν_1, ν_2 and κ are independent of the triangulation.